Journal of Alloys and Compounds 1009 (2024) 176966

Contents lists available at ScienceDirect

Journal of Alloys and Compounds

journal homepage: www.elsevier.com/locate/jalcom

Unraveling the structural and thermoelectric properties of the Sn-doped filled skutterudite $Sm_y(Fe_xNi_{1-x})Sb_{11.5}Sn_{0.5}$ ($y = 0.17–0.34$, $x = 0.43–0.64$)

Cecilia Piscino [a], Giovanna Latronico [b,c], Pietro Manfrinetti [a,d], Nadia Parodi [a], Roberto Spotorno [a], Carlo Fanciulli [b], Ketan Lohani [e,1], Tanguy Bernard [e], Paolo Scardi [e], Paolo Mele [c], Cristina Artini [a,f,*]

[a] Department of Chemistry and Industrial Chemistry, University of Genova, Genova 16146, Italy
[b] Institute ICMATE, CNR, Lecco 23900, Italy
[c] College of Engineering - Shibaura institute of Technology, 307 Fukasaku, Minuma-ku, Saitama 337-8570, Japan
[d] Institute SPIN, CNR, Genova, Genova 16152, Italy
[e] Department of Civil, Environmental and Mechanical Engineering, University of Trento, Trento 38123, Italy
[f] Institute ICMATE, CNR, Genova 16149, Italy

ARTICLE INFO

Keywords:
Thermoelectricity
Filled skutterudites
Crystal structure
Seebeck coefficient
Thermal conductivity

ABSTRACT

A systematic study of the filled skutterudite system $Sm_y(Fe_xNi_{1-x})_4Sb_{11.5}Sn_{0.5}$ was carried out with the aim of investigating the effect of the partial substitution of Sb by Sn on the structural and thermoelectric properties of the material. The presence of Sn induces a shift of the *p/n* crossover toward lower values of *x* compared to the corresponding Sn-free system, as a consequence of the smaller number of electrons supplied. Moreover, a discontinuity at the *p/n* crossover is observed in the cell parameter and related structural features. The thermoelectric properties suggest lower thermal conductivity values in comparison to similar Sn-free skutterudite systems, resulting in higher *ZT*. This result highlights the significant role of Sn in creating new scattering centers able to affect the phonon transmission through the crystal lattice.

1. Introduction

Thermoelectricity is commonly considered as a valid energy harvesting technology, which allows recovering waste heat by converting it directly into electricity [1−5]. Applications range from thermoelectric radioisotope generators for space explorations [6] to hybrid solar-thermoelectric generators [7,8], thermoelectric coolers [9,10], wearable technology [11], thermal energy conversion in buildings [12], and green hydrogen production [13]. Waste heat can come from a variety of sources, such as industrial activity or home, and even from the human body: the wide temperature range covered by such different environments requires the use of different thermoelectric materials [14,15]. Thermoelectric modules are made of several high-performance *p*- and *n*-type semiconductor legs, electrically connected in series and thermally in parallel. The performance of such modules depends on the thermoelectric performance of the materials of each individual leg, which is estimated by the so-called figure of merit (*ZT*), defined as

$$ZT = \left(\sigma S^2\right) \quad T/(k_{ph} + k_{el}) \tag{1}$$

where σ is the electrical conductivity, S the Seebeck coefficient, T the absolute temperature, k_{ph} and k_{el} the phonon and electron thermal conductivity, respectively, and the product ($S^2\sigma$) the power factor (*PF*).

A high *ZT* can be achieved either by increasing the power factor (*PF*) or by suppressing the thermal conductivity. Even if both approaches are feasible, from the experimental viewpoint the latter is more readily achievable, since it mainly involves the introduction and engineering of scattering centers, which contribute to the reduction of the phonon thermal conductivity by reducing the phonon mean free path [16,17]. This approach, leaving k_{el}, and consequently σ, intact, follows the well-known PGEC (Phonon Glass Electron Crystal) concept [18], stating that ideal thermoelectric materials should conduct heat like glass and electricity like a crystal.

Several materials are currently studied in this context, such as organic materials [19], and among inorganic ones, half Heusler phases [20,21], chalcogenides [22,23], clathrates [24], and high-entropy alloys

* Corresponding author at: Department of Chemistry and Industrial Chemistry, University of Genova, Genova 16146, Italy.
E-mail address: cristina.artini@unige.it (C. Artini).
[1] Present address: Institute of Micro and Nanotechnology IMN-CNM (CSIC), 28760 Madrid, Spain.

https://doi.org/10.1016/j.jallcom.2024.176966
Received 15 July 2024; Received in revised form 9 October 2024; Accepted 10 October 2024
Available online 11 October 2024

[25,26]. In addition to the mentioned material classes, filled skutterudites are ideal candidates to be optimized as thermoelectric materials, since they possess a reasonably high power factor (on average around 1.5–2 mW/mK^2), and can be easily manipulated through the introduction of guest atoms, which significantly lower phonon thermal conductivity [27–29]. Skutterudites MX_3 (M ≡ transition element, for example Co, Fe, Rh or Ir, and X ≡ pnictide atom), crystallize in a body-centered cubic cell (space group: $Im\bar{3}$, isotypic crystal: $CoAs_3$). The two crystallographic positions, namely the 8*c* (¼, ¼, ¼) and the 24 *g* (0, *y*, *z*), are populated by M and X, respectively: an icosahedral cavity X_{12} is therefore formed with its center in 2*a* (0,0,0).

In general, scattering centers can be of different nature, namely point defects (vacancies, susbstitutional or interstitial atoms), nano-precipitates [30], grain boundaries, dislocations, pores [31] and so on; in this respect, the dimensionality reduction through thin film deposition [32] also plays a role in the suppression of k_{ph} due to the strain arising at the substrate/film interface [33,34]. In the particular case of filled skutterudites, scattering centers are mainly guest atoms occupying the 2*a* position at the center of the cavity. This cage, generally oversized with respect to the cations, is able to retain, even if through loose bonds, the largest lanthanide and alkaline earth ions, thus achieving at least a partial filling. The guest cations vibrate around their equilibrium positions, giving rise to a rattling motion which strongly lowers k_{ph}. Based on this, many different filled skutterudites have been synthesized: even limiting to Sb-based skutterudites, filling with Sm [35], Ce [36] and Yb [37] has been attempted. Furthermore, since multifilling is even more effective, this approach has also been explored, and DD (DD ≡ didymium, a Pr/Nd mixture) [38], Mm (Mm ≡ mischmetal) [39], Sm/Gd [40], and Ba/Sr/Pr/Nd/Yb [41] have been satisfactorily used as filler mixtures. In addition to multifilling, the partial substitution of Co by another transition element, as well as its total substitution by a pair of different metals, has also been attempted with the aim of inserting additional scattering centers, leading, for example, to the synthesis of Fe/Co [42-45], Co/Ni [46-48], Fe/Ni [28,40,49,50], and Fe/Co/Ni [39, 51] skutterudites. A further path to be pursued with the aim of reducing k_{ph} in filled skutterudites is the introduction of scattering centers by partial substitution of Sb with one or more aliovalent elements, such as Sn [52,53], Ge [42,54], Te [55,56], Se [57], Se/Te [57,58], Te/S [59], or Te/Sn [60,61]; this approach is expected to be particularly effective, since the heat-carrying phonons in skutterudites are associated with the vibrational modes of the Sb rings, so a disordering effect on the latter should strongly influence the phonon thermal conductivity [62-64].

All the above-mentioned substitutions exert an effect not only on the thermal transport of the material, but also on its electronic properties, *i.e.* on the conduction regime of skutterudite. Even without resorting to band structure calculations, the electronic structure of the parent skutterudite $CoSb_3$ can be correctly described according to the Zintl concept, which predicts that the compound is a compensated semiconductor with diamagnetic properties [27], as indeed experimentally observed. The introduction of a guest cation in 2*a*, contributing a certain number of electrons, is difficult to achieve [65], due to the high stability of the compound. Electron-deficient skutterudites, such as those with Co partly or totally replaced by a lighter transition element, on the contrary, require an electron contribution to reach stability. This is the case, for instance, of Fe/Ni- [35] and Co/Ni- [39] based skutterudites, which host a certain amount of filler cations that do not perfectly counterbalance the electron requirement of a compensated semiconductor, thus giving rise to *p*- and *n*- compounds. Partial substitution of Sb with an aliovalent element also influences the electronic count of the compound. In particular, the introduction of Sn, an atom characterized by an electron less than Sb in the outer shell, determines a broadening of the *p*-region by shifting the *p*/*n* crossover toward a lower Fe content, as already observed in previous preliminary studies conducted on $Sm_y(Fe_xNi_{1-x})Sb_{12-\delta}Sn_\delta$ [66] and $CoSb_3$-$_\delta Sn_\delta$ [67].

In this work a systematic study performed on several samples belonging to $Sm_y(Fe_xNi_{1-x})Sb_{11.5}Sn_{0.5}$ is described with the aim of investigating the effect of the partial substitution of Sb by Sn on the electronic and thermoelectric properties of the system, as well as to correlate these features with the average crystal structure of the skutterudite. The results are discussed in comparison with those deriving from the corresponding Sn-free system [35] and other similar skutterudite systems.

2. Material and methods

2.1. Synthesis

Seven samples belonging to the $Sm_y(Fe_xNi_{1-x})_4Sb_{11.5}Sn_{0.5}$ system with $0.43 \leq x \leq 0.64$, and $0.17 \leq y \leq 0.34$ (characterized by a progressive and concomitant increase in both Fe and Sm: $x = 0.43, 0.45, 0.47, 0.50, 0.54, 0.58, 0.64$; $y = 0.17, 0.19, 0.20, 0.23, 0.26, 0.26, 0.34$) were synthesized by the melting-quenching-annealing technique. The synthesis was performed starting from the pure elements Fe (Alfa-Aesar, 99,99 wt%), Ni (NewMet, 99.9 wt%), Sn (Sigma Aldrich, 99.99 wt%), Sb (Mateck, 99.999 wt%), and from the precursor compound $Sm_{0.15}Sb_{0.85}$ previously prepared. Reagents were placed in quartz ampoules and then sealed under vacuum. The synthetic process consisted in a thermal treatment at 1223 K for 1 hour to allow the reagents to melt and react, followed by rapid cooling in air. Subsequently, an annealing treatment was performed at 873 K for 10 days.

The precursor compound $Sm_{0.15}Sb_{0.85}$ was obtained by reacting Sb with Sm (NewMet, 99.9 wt%) in a sealed Ta crucible placed in an induction furnace; it was used to increase the homogeneity of the final samples and to minimize the Sm losses due to oxidation during the melting treatment.

The compositions were chosen in order to synthesize both *p*-type and *n*-type skutterudites; the Sm content, *i.e.* the *y* value, was selected in agreement with the results obtained in [66]. Samples were named Fe43_Sn, and so on, based on the Fe content in % in relation to the total amount of (Fe + Ni).

2.2. Optical and electron microscopy

A preliminary view of the vertical section of the specimens was obtained by optical microscopy, with a LEICA ICC50 W. Then, the samples were sputter-coated with a 6 nm thick gold layer on the surface and observed by scanning electron microscopy (Cambridge INCA 300 with PentaFET EDS detector sensitive to light elements, $Z > 5$, Oxfordshire, UK), coupled with EDS microprobe to obtain information on their composition and morphology. Before the compositional analysis, a quantitative optimization procedure was carried out using a Co standard (99.995 wt%) in order to correct the filament current and the beam spot size on the sample. Images of the samples were collected using both backscattered and secondary electrons.

2.3. X-ray diffraction

The samples were ground and sieved trough a 44 μm mesh sieve to obtain homogeneous powders, which were placed on a zero-background Si sample-holder and analyzed by a Bragg-Brentano powder diffractometer equipped with a Cu anticathode (Bruker D4 Endeavor, Cu Kα radiation). XRD patterns were collected in the range $10° < 2\theta < 100°$ with angular step 0.02°, 1 s per step. The refinement of the structural models was performed with the Rietveld method using the FullProf software [68].

2.4. Differential scanning calorimetry (DSC)

Thermal characterization of the specimens was performed by differential scanning calorimetry (DSC) with a LABSYS Evo to evaluate the

decomposition temperature of the skutterudite, and with a SETARAM DSC11 to measure heat capacity (C_p).

The former analyses were carried out from 303 K to 1123 K on powders in a sealed Ta crucible under Ar atmosphere. The heating rate in the 303–473 K range was set at 10 K/min, while from 473 K to 1123 K it was reduced to 5 K/min. Then samples were cooled down to room temperature at 10 K/min.

C_p measurements were performed by a Calvet calorimeter. The reference and the working cell, surrounded by two thermopiles, were subjected to a temperature program from room temperature to 773 K. The investigation involved three steps: a) the implementation of a 'zero test', performed by using two identical empty sample holders to reveal the possible heat flux difference between the reference and working cells; b) the experimental test performed with the sample in the experimental cell; c) the calibration with Al_2O_3 as a standard. To ensure the reliability of the experimental results, the investigation was performed at constant heating rate and uniform Ar flow, and within an equally scanned temperature range.

2.5. Measurement of transport properties

The Seebeck coefficient (S) at room temperature was measured by a home-made instrument that provides the voltage produced by the sample under the application of a stable temperature difference of about 10 K.

To perform transport measurements as a function of temperature, bulk specimens were ground, sieved and pressed in rectified presses; pellets with a diameter of 10 and a thickness of 1.5 mm were obtained. Then, disks were inserted into glass ampoules subsequently sealed under vacuum and sintered at 823 K for 7 days to reduce the porosity of the starting material; the density of the sintered pellets ranges between 80 % and 90 %. S and resistivity (ρ) were then simultaneously measured in the temperature range 323–723 K using a Linseis Messgeraete GmbH LSR-3 instrument under He atmosphere in a four-contact configuration.

The thermal diffusivity (α) of 5 specimens (Fe43_Sn, Fe45_Sn, Fe47_Sn, Fe54_Sn, Fe64_Sn) was measured on the same disk samples under low vacuum and in the same temperature range as S and ρ. These measurements were carried out using a Linseis Messgeraete GmbH LFA-500 light flash instrument equipped with a Xe lamp. The thermal conductivity (k) was calculated *via* the following equation:

$$k = \alpha \cdot d \cdot C_p \tag{2}$$

where d is the sample density, and C_p is the specific heat at constant pressure.

The uncertainties associated with the measurements are 7 % for the Seebeck coefficient, 7 % for the electrical resistivity, 9 % for thermal conductivity, and 30 % for the figure of merit.

3. Results

3.1. Morphological, structural and compositional characterization

Scanning electron microscopy images reveal a high porosity of the annealed samples; moreover, in addition to the filled skutterudite, which is by far the main phase, small amounts of extra phases, such as (Fe,Ni)Sb_2 and $Sb_{1-z}Sn_z$, can be detected in some samples. The former appears from $x = 0.54$, and its amount slightly increases with the increase of Fe content (a table collecting the amount of extra phases for each sample, as revealed by EDS, is reported in the Supplementary Material). The latter is a solid solution formed due to the size similarity of Sb and Sn; depending on the sample, the Sn amount within $Sb_{1-z}Sn_z$ ranges between 1 and 9 at%. Fig. 1a, for example, shows the polished surface of the Fe47_Sn sample: the presence of holes (black regions) and of some needle-like crystals of $Sb_{1-z}Sn_z$ dispersed inside the skutterudite matrix is visible. According to SEM micrographs, the average size of skutterudite crystals is about 10 μm, as can be observed in Fig. 1b, where crystals grown inside a surface hole of the Fe47_Sn sample can be seen.

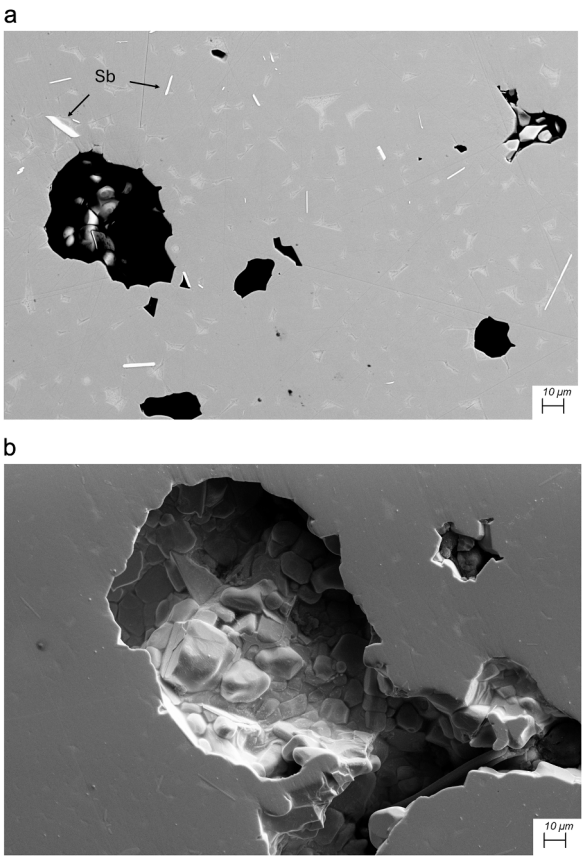

Fig. 1. SEM microphotograph taken on the polished surface of Fe47_Sn a) by backscattered electrons and b) by secondary electrons.

The superimposed diffraction patterns of all samples are shown in Fig. 2; the skutterudite reference diffractogram is contained in the entry no. 1530708 of the Pearson's Crystal Database [69]. The diffraction data were analyzed with the Rietveld method by optimizing a structural model containing the filled skutterudite phase, and, when necessary, incorporating additional phases. The background of each diffractogram was modeled by fitting ~70 experimental points selected from the collected pattern; the peak profiles were modelled by pseudo-Voigt functions. In the last rounds of refinement, the structural parameters of the skutterudite (the lattice parameter, the atomic x and y coordinates of Sb, as well as the Sm occupancy in the crystallographic site 2a), the nine peak parameters, the scale factor and the background points, were simultaneously refined. The amounts of each element within the filled skutterudite were determined as follows. The Sm occupancy factor was obtained by Rietveld refinements by alternatively optimizing the 2a occupancy factor and the Sm isotropic displacement parameter (B_{iso}); this procedure was followed to avoid correlation effects, until both parameters converged to a stable value. Subsequently, they were allowed to vary simultaneously: since they did not change significantly, it was possible to confirm that they had reached stability. Fe and Ni occupancies were fixed at the value obtained from EDS and not allowed to vary due to the similarity of their scattering factors. The overall occupancy of the 24 g position, *i.e.* the one populated by Sb and Sn, was considered full, based on the results of both EDS and Rietveld refinements. The amounts of Sb and Sn were fixed at the value provided by EDS; when allowed to vary during refinements, they proved to be stable, which confirmed the stability of the refinement process and the correctness of the structural model. Fig. 3 reports the Rietveld refinement plot of Fe64_Sn; Table 1 collects the agreement factors, as well as the

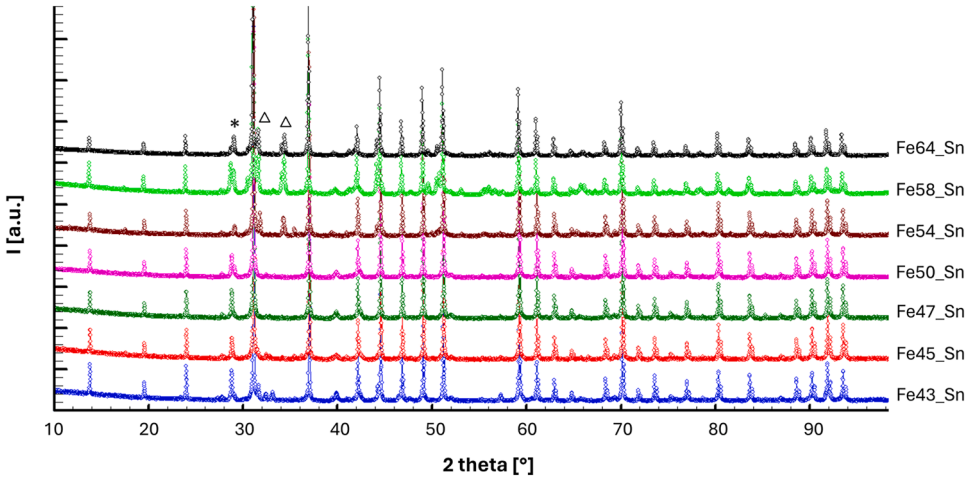

Fig. 2. Diffraction patterns of all the samples displayed in a stacked sequence. Asterisks and triangles mark the presence of $Sb_{1-z}Sn_z$ and $(Fe,Ni)Sb_2$, respectively.

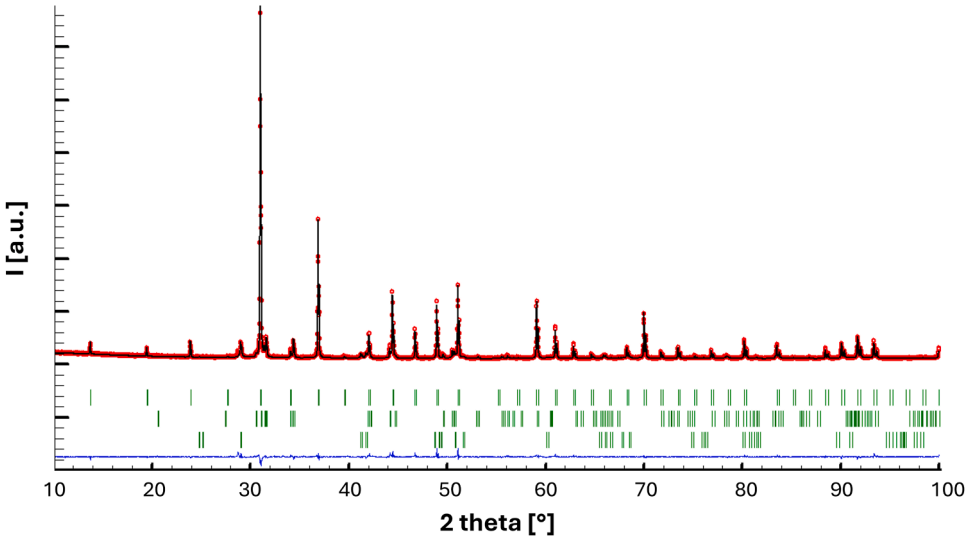

Fig. 3. Rietveld refinement plot of Fe64_Sn. The red dotted and the black continuous lines are the experimental and calculated pattern, respectively; the blue line at the bottom is the difference curve. Green vertical bars correspond to the calculated positions of Bragg peaks of the different phases (from top to bottom: skutterudite; $(Fe,Ni)Sb_2$; $Sb_{1-z}Sn_z$).

Table 1
Nominal and refined composition, Rietveld agreement factors and energy gap (E_g) for each sample.

Sample	*Nominal composition*	*Refined composition*	χ^2	R_B	E_g *[meV]*
Fe43_Sn	$Sm_{0.15}(Fe_{0.35}Ni_{0.65})_4Sb_{11.50}Sn_{0.50}$	$Sm_{0.17}(Fe_{0.43}Ni_{0.57})_4Sb_{11.63}Sn_{0.37}$	9.37	9.54	109
Fe45_Sn	$Sm_{0.18}(Fe_{0.40}Ni_{0.60})_4Sb_{11.50}Sn_{0.50}$	$Sm_{0.19}(Fe_{0.45}Ni_{0.55})_4Sb_{11.54}Sn_{0.46}$	8.66	9.14	108
Fe47_Sn	$Sm_{0.22}(Fe_{0.45}Ni_{0.55})_4Sb_{11.50}Sn_{0.50}$	$Sm_{0.20}(Fe_{0.47}Ni_{0.53})_4Sb_{11.60}Sn_{0.40}$	10.10	10.05	94
Fe50_Sn	$Sm_{0.23}(Fe_{0.50}Ni_{0.50})_4Sb_{11.50}Sn_{0.50}$	$Sm_{0.23}(Fe_{0.50}Ni_{0.50})_4Sb_{11.58}Sn_{0.42}$	8.88	9.66	48
Fe54_Sn	$Sm_{0.26}(Fe_{0.55}Ni_{0.45})_4Sb_{11.50}Sn_{0.50}$	$Sm_{0.26}(Fe_{0.54}Ni_{0.46})_4Sb_{11.56}Sn_{0.44}$	10.8	10.91	122
Fe58_Sn	$Sm_{0.27}(Fe_{0.60}Ni_{0.40})_4Sb_{11.50}Sn_{0.50}$	$Sm_{0.26}(Fe_{0.58}Ni_{0.42})_4Sb_{11.61}Sn_{0.39}$	10.4	3.93	75
Fe64_Sn	$Sm_{0.34}(Fe_{0.65}Ni_{0.35})_4Sb_{11.50}Sn_{0.50}$	$Sm_{0.34}(Fe_{0.64}Ni_{0.36})_4Sb_{11.60}Sn_{0.40}$	3.46	4.32	92

nominal and experimental composition of the filled skutterudite in the seven samples (with the latter deriving from the combined results of EDS and XRD analyses, as previously described), and the energy gap (E_g), which will be discussed later; the raw data provided by EDS are collected in the Supplementary Material.

The first interesting result comes from the comparison between nominal and experimental compositions. It can be observed that the largest discrepancy between the two values occurs at low Fe content, with the nominal amount being lower than the experimental one. This evidence finds an explanation considering that x values lower than 0.50 in $Sm_y(Fe_xNi_{1-x})_4Sb_{12}$ are close to the boundary of the skutterudite stability region, as shown in [35], where the lowest experimental x was 0.37. Based on the Zintl model, the introduction of Sn is expected to enlarge the skutterudite stability region, as described in more detail in the Discussion; in any case, the present result suggests that $x \sim 0.40$ represents the lower limit of the Fe content.

A further conclusion to be drawn from the comparison of nominal and experimental compositions concerns the Sn content of the samples.

In contrast to the nominal stoichiometric amount of Sn, which is 0.5 for each formula unit, the experimental amount is always slightly lower, ranging between 0.37 and 0.46. It is worth noting that Fe64_Sn is the sample with the highest Fe content hosting Sn at the Sb site; all attempts to synthesize Sn-containing samples with higher Fe content were unsuccessful.

The most direct result from the Rietveld refinements is the trend of the cell parameter as a function of the Fe content. This plot, reported in Fig. 4, similarly to what has already been observed in other similar systems [35,40], is characterized by a linearly increasing behaviour with increasing x, due to the larger ionic size of Fe with respect to Ni. Again, and in in analogy with the corresponding Sn-free skutterudite [35], as well as with the (Sm,Gd)-filled one [40], a change in slope occurs: in the present system it takes place at $x \sim 0.53$.

A further significant refined parameter provided by the Rietveld method is the atomic displacement parameter (B_{iso}) of the filler atom. Its behaviour, reported in Fig. 5, is indeed typical of filled skutterudites, as it assumes particularly high values at low Fe content, and strongly decreases with increasing x; however, it remains quite high even at high Fe content when correlated with the large atomic weight of Sm. This feature, common to other similar systems [35,40], can be explained taking into account that two main factors contribute to B_{iso}, namely dynamic and static disorder. The first is triggered by thermal agitation; the latter, on the contrary, can be associated with the presence of more than one atomic species in an atomic site, or with an incomplete occupation of the site. In filled skutterudites the contribution of the filler atom to the dynamic disorder, despite its high atomic mass, is quite high at every composition, being it located inside an oversized cage, and therefore weakly bound to the 12 Sb atoms. However, the major contribution comes from the static disorder, due to the very low occupancy factor of the 2*a* position. This evidence can be verified by observing the trend of the refined values of y *vs.* x for both the Sn-doped and the Sn-free system [35], reported in Fig. 6: they show a linear increase in the amount of Sm (y), as a response to the need for a progressively greater electron supply due to the progressive substitution of Ni^{4+} with Fe^{2+}. In particular, the very low values of y at low Fe amount are responsible for the very high values of the Sm B_{iso} at low x. It should be noted at this point that the assignment of the 4+ oxidation state to Ni [27] has not been confirmed experimentally; however, it works very well in predicting the position of the p/n crossover in (Fe,Ni)-based skutterudites [35], as will be described in more detail in the Discussion, and is therefore generally accepted.

The DSC curves collected on all the samples are reported in Fig. 7. A similar behaviour is observed for all compositions, with two endothermic signals occurring in the temperature range 890–900 K and

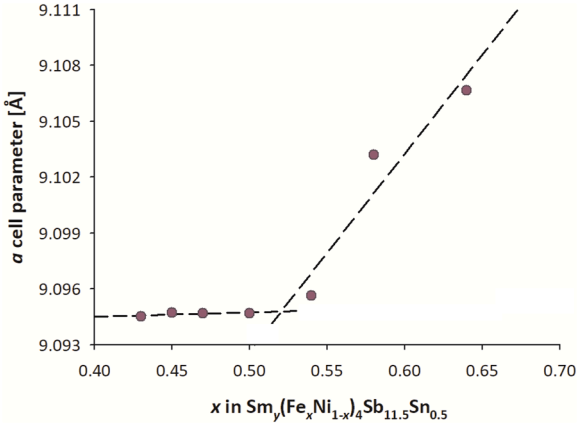

Fig. 4. Trend of the cell parameter as a function of x in $Sm_y(Fe_xNi_{1-x})_4Sb_{11.5}Sn_{0.5}$. The two different data sets ($0.43 \leq x \leq 0.54$ and $0.54 \leq x \leq 0.64$) are fitted by two different regression lines. Error bars are hidden by data markers.

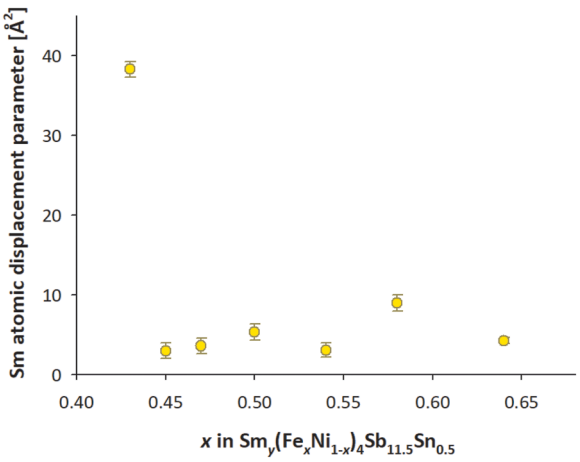

Fig. 5. Atomic displacement parameter (B_{iso}) of Sm as a function of the Fe amount (x).

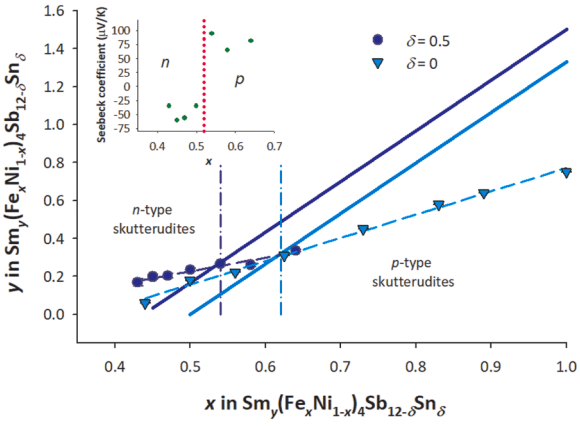

Fig. 6. Trend of Sm *vs.* Fe content (y *vs.* x) for both Sn-doped and Sn-free samples. The latter data are those from ref. [27]. Error bars are hidden by data markers. Inset: data of room temperature Seebeck coefficient for Sn-doped samples.

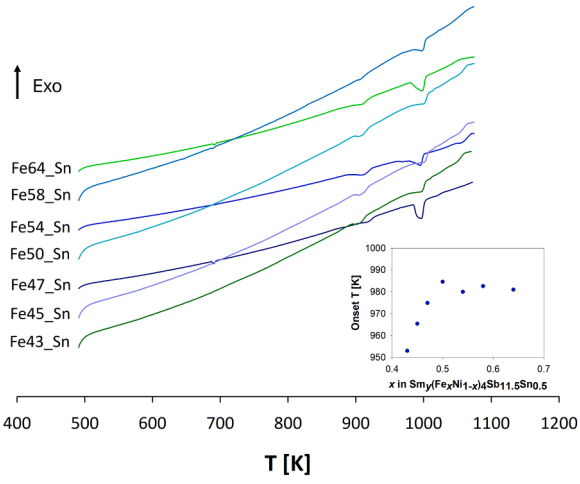

Fig. 7. DSC curves of samples belonging to the $Sm_y(Fe_xNi_{1-x})_4Sb_{11.5}Sn_{0.5}$ system collected during heating. Inset: onset temperature of decomposition as a function of the Fe content.

950–980 K, respectively, the one at the higher temperature being the most intense. The inset to Fig. 7 reports the trend of the onset temperature of the latter signal as a function of the Fe content x. The stability of the filled skutterudite will be analyzed in detail in the Discussion section.

3.2. Thermoelectric characterization

The Seebeck coefficients as a function of temperature are reported in Fig. 8. Based on their sign, it can be concluded that up to $x = 0.50$ samples are n-conductors, while at higher Fe content they are p-conductors. In this regard, the position of the p/n crossover can be identified between $x = 0.50$ and $x = 0.54$. All compositions exhibit a maximum in the absolute value of the Seebeck coefficient; this trend is quite common in semiconductors, and generally reflects a similar behaviour of the electrical resistivity. This pattern concerns the fact that at low temperature extrinsic charge carriers prevail, while beyond the maximum electron–hole pairs are excited across the energy gap. The presence of the maximum allows the estimation of the energy gap (E_g) *via* the Goldsmid and Sharp equation [70]

$$S_{max} = \frac{E_g}{2eT_{max}} \quad (3)$$

where e is the electron charge, S_{max} and T_{max} are the maximum value of S, and the temperature where the maximum occurs, respectively; S_{max} and T_{max}were evaluated by fitting experimental data to a fourth order polynomial function. According to this expression, the E_g values reported in Table 1 were found.

The resistivity data, reported in Fig. 9, reveal a weak temperature dependence, with the only exception of Fe50_Sn and Fe54_Sn, *i.e.* the samples in the immediate vicinity of the p/n crossover. The last-mentioned compositions show in fact a marked semiconducting behaviour, implying higher resistivity values compared to other samples and a decreasing trend of resistivity almost through the entire temperature range explored. At lower and higher Fe contents, a more pronounced n- and p-character develops, respectively, and a maximum in the resistivity trend of ρ *vs.* T occurs, indicating a progressive change from metallic to semiconducting behaviour with increasing temperature; the maximum shifts towards lower temperatures approaching the p/n crossover from both directions. All these features are quite common in Fe/Ni filled skutterudites, since they have already been observed in other similar systems, such as (Sm,Gd)- [40], DD- (DD ≡ didymium) [71], (Ba,Sr,DD,Yb)- [41], and Yb- [37] filled $(Fe_{1-x}Ni_x)_4Sb_{12}$ skutterudites. The occurrence of the above maximum, hence of the transition from a metallic to a semiconducting regime, is consistent with a shift of the Fermi level towards the band gap as the p/n crossover approaches. Furthermore, the shift of the metal/semiconductor threshold towards

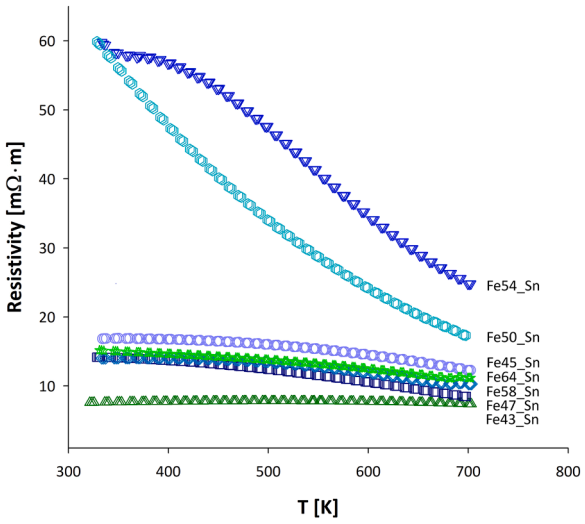

Fig. 9. Trend of the electrical resistivity as a function of temperature.

lower temperatures as the p/n crossover approaches, is most likely related to the band gap contraction already observed for similar systems [71]. Indeed, resistivity and Seebeck are in good agreement, since the minimum temperature of T_{max} recorded in resistivity occurs in proximity to the minimum value of the calculated energy gap, as evident from the comparison with data reported in Table 1.

The combined effect of electrical conductivity (σ) and S gives rise to the behaviour of the power factor (PF), reported in Fig. 10 as a function of temperature. All data series present a maximum, whose position (T_{max}) changes with the Fe content x. In particular, T_{max} takes the minimum value close to the p/n crossover, which, according to Seebeck measurements, is located between $x = 0.50$ and $x = 0.54$. Interestingly, the behaviour of T_{max} *vs.* Fe content, represented in Fig. 11 for resistivity, Seebeck coefficient, power factor, and ZT, is approximately similar for all these properties.

The thermal conductivity k of the five samples listed in paragraph 2.5 is reported as a function of temperature in Fig. 12. All data series are characterized by an increasing trend, in good agreement with other similar systems [40,71]. It is also interesting to note that the higher the Sn content actually entering the structure, the lower the thermal conductivity, as deduced from the low k values of Fe45_Sn and Fe54_Sn, which, according to the data collected in Table 1, contain the highest amount of Sn among all the studied compositions. The attribution of the k reduction to the introduction of Sn into the structure is confirmed by the trend of the phonon thermal conductivity k_{ph}. This parameter, reported in Fig. 13, was calculated by subtracting the electron

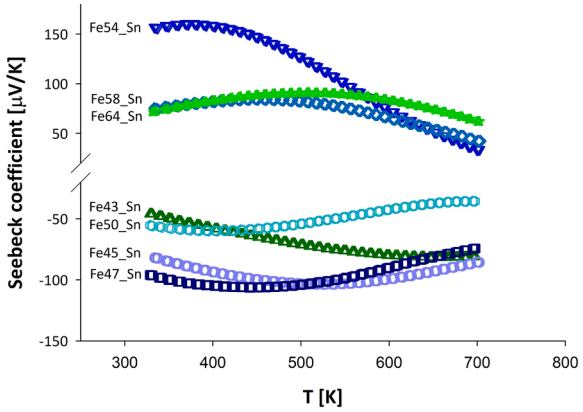

Fig. 8. Trend of the Seebeck coefficient as a function of temperature.

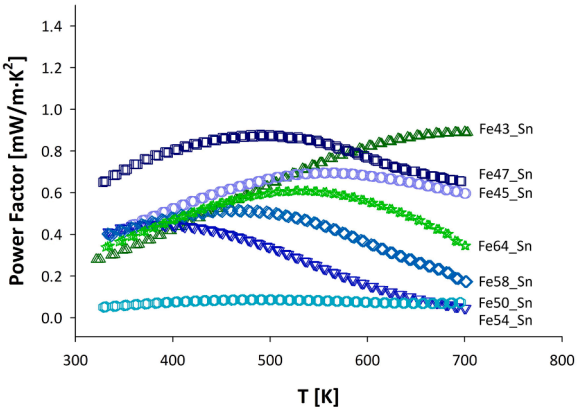

Fig. 10. Trend of the power factor as a function of temperature.

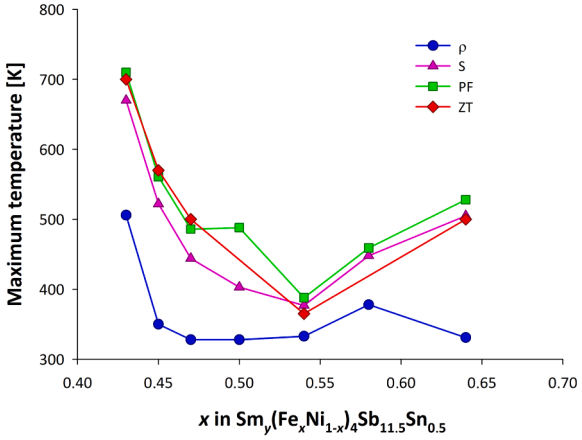

Fig. 11. Trend of T_{max} *vs.* the Fe content for resistivity, Seebeck coefficient, power factor, and *ZT*.

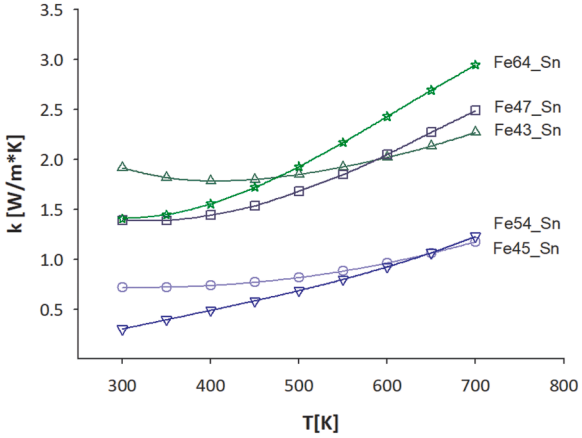

Fig. 12. Trend of the overall thermal conductivity as a function of temperature.

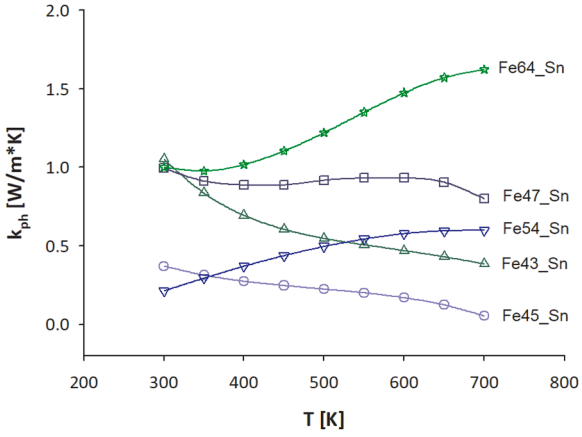

Fig. 13. Trend of the phonon thermal conductivity as a function of temperature.

contribution k_{el} from the overall thermal conductivity. To do this, the Wiedemann-Franz law

$$k_{el} = \frac{L_0}{\rho} T \tag{4}$$

was used, where L_0 is the Lorenz number, calculated through the Seebeck coefficient, as suggested in [72]. The particularly low value of k_{ph} is confirmed for the two above-mentioned samples, suggesting that this effect is most likely due to the partial substitution of Sb with Sn through the reduction of the phonon mean free path.

All the described properties contribute to *ZT*, which is plotted as a function of temperature in Fig. 14. As expected from the particularly low *k* values of Fe45_Sn and Fe54_Sn, the highest *ZT* values are indeed exhibited by these compositions. All data show a maximum, the position of which is close to that observed in the *PF* trend.

4. Discussion

The evaluation of the structural and thermoelectric properties of the $Sm_y(Fe_xNi_{1-x})_4Sb_{11.5}Sn_{0.5}$ system cannot ignore the question of the thermodynamic stability of the skutterudite. To gain insight into this point, the results of DSC measurements are discussed in comparison with those obtained on Sn-free samples [73] taking as a reference the ternary Fe-Ni-Sb diagram, and in particular the pseudobinary $Fe_{25}Sb_{75}$-$Ni_{25}Sb_{75}$ phase diagram [74]' reproduced in Fig. 15. According to the latter work, the monophasic stability field of unfilled skutterudite (η) is quite narrow, since it only extends around the Fe/Ni equimolar composition for a few percent. However, the field broadens with the insertion of a filler ion, such as Sm [73], even if it is not entirely clear whether the extra phases Sb and (Fe,Ni)Sb_2 found in Sm-filled skutterudite at $x > 0.63$ and $x < 0.50$ are in equilibrium or metastable. Again according to [74], beyond the compositional limits of the monophasic field, the skutterudite is stable together with Sb and (Fe,Ni)Sb_2 (ε); furthermore, it is formed through the following two peritectic reactions:

$$1018\ \text{KL} + \delta \rightarrow \varepsilon \tag{5}$$

$$915\ \text{KL} + \delta + \varepsilon \rightarrow \eta \tag{6}$$

where η is the skutterudite, ε is (Fe,Ni)Sb_2, and δ is (Fe,Ni)Sb.

In the light of these considerations, the endothermic signal occurring in the thermograms of the Sn-doped system at lower temperature (see Fig. 7) can be associated with Eq. 6, while the one at higher temperature refers to Eq. 5. Compared to the unfilled skutterudite [74], and even to the Sn-free system [73], the Sn-doped skutterudite studied in this work exhibits both reactions at slightly lower temperatures. The knowledge of the decomposition temperature of skutterudite is of great significance to keep the annealing temperature below this threshold. Regarding the stability of the observed extra phases, it is indeed not clear whether they are in thermodynamic equilibrium or not; in other words, the position of the boundary between the (η) and the (Sb + ε + η) fields is doubtful. As to this, a previous study performed on the corresponding Sn-free skutterudite may be helpful [50]. According to this study, the rapid solidification of the samples induces the disappearance of the extra phases in the compositions with *x* between 0.50 and 0.70; in the Sn-doped system,

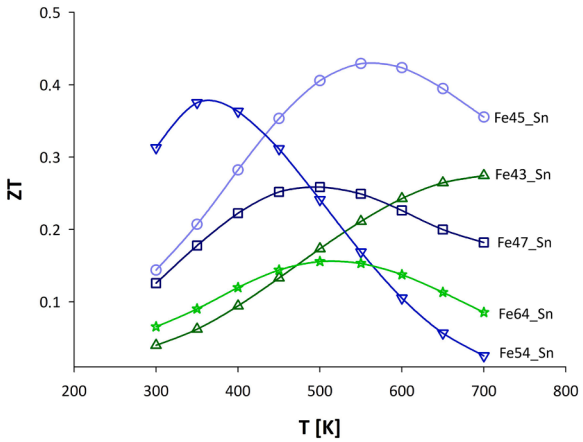

Fig. 14. Trend of *ZT* as a function of temperature.

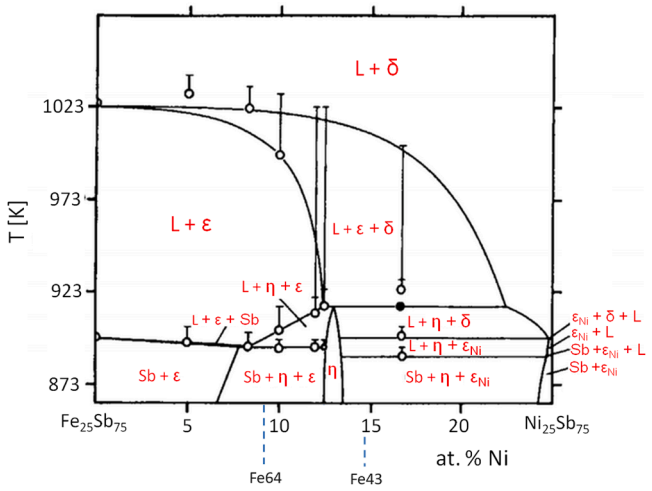

Fig. 15. Isopleth at 75 at% Sb of the ternary diagram Fe-Ni-Sb. η: skutterudite; ε: Fe-rich (Fe,Ni)Sb_2; ε_{Ni}: Ni-rich (Fe,Ni)Sb_2; δ: (Fe,-Ni)Sb. The compositional range studied in this work is indicated. Reproduced from ref. [61]; original data derive from ref. [62].

the skutterudite stability region is apparently narrower and shifted toward lower x values.

The refined values of the Sm y content, reported in Fig. 6 for the Sn-doped and the Sn-free system [35] as a function of the amount of Fe x, show an increasing trend, indicating a progressive filling of the 2a position. This evidence is in good agreement with the increasing demand for electrons caused by the substitution of Ni^{4+} with Fe^{2+}, as well as with the cage dimensions with increasing amount of Fe. However, the electronic count shows that the number of electrons supplied by the filler ion does not exactly match the amount of charge needed by both systems to reproduce the electronic count of a compensated semiconductor, such as $CoSb_3$. Instead, the electron content is highest at low x values and lowest at high x values, thus giving rise to n- and p-skutterudites, respectively. In particular, in Fig. 6 the solid lines represent the ideal y values needed to reproduce the electronic count of a compensated semiconductor, calculated assuming that Fe and Ni are respectively in the 2+ and 4+ oxidation state [27], as previously discussed; the dashed lines fit experimental data. For each of the two systems the two lines cross at a composition corresponding to the p/n crossover as predicted by the structural analysis. The prediction is well confirmed by the measurement of Seebeck coefficient at room temperature, reported in the inset for the Sn-doped system, and in ref. [35] for the Sn-free one: the maximum value of S, corresponding to the composition in which the charge carrier density reaches its minimum, is found in the first system between $x = 0.50$ and $x = 0.54$, *i.e.* where it is predicted based on the structural analysis. In the latter it occurs in the vicinity of $x = 0.63$, which again corresponds to the position of the crossover predicted by the structural analysis for that system [35]. The shift of the crossover toward lower x values with the partial replacement of Sb with Sn occurs as a consequence of the smaller number of electrons contributed by Sn compared to Sb. This problem is of particular interest when designing a thermoelectric module, since the knowledge of the conduction regime of the material is of fundamental importance.

The p/n crossover also leaves its mark in several structural parameters, further confirming its position. Similarly to what was observed in the Sn-free system, [35] also in the present one a change of slope in the trend of the cell parameter as a function of the Fe content occurs at x, as can be deduced from Fig. 4. This evidence, whose origin is still not completely clear, is most likely attributable to a change in the Fe spin state that occurs at the crossover. A similar discontinuity can also be observed in the interatomic distance Sm-(Sb,Sn), which shows a sharp increase near $x = 0.50$, following the trend of the cell parameter; this

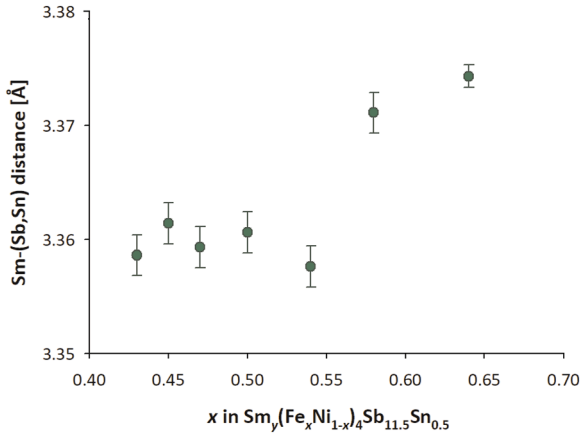

Fig. 16. Trend of the Sm-(Sb,Sn) interatomic distance as a function of the Fe content x.

behaviour can be observed in Fig. 16.

The sum of the fractional coordinates y and z of the 24 g position, occupied by the pnictide atom, is a further significant structural parameter, being an indicator of the proximity to the ideal condition of complete filling of the 2a position, as stated by Oftedal [75] and later partly amended by Kjeksus *et al.* [76]. The sum $(y + z)$ tends in fact to 0.5 as the full occupancy of the 2a-centered cages in Sb-based filled skutterudites approaches; when this value occurs, the groups of four neighbouring Sb atoms assume a square shape, while for any other value they are rectangular. More generally, in all filled skutterudites this parameter increases with increasing filling degree at site 2a. Interestingly, unlike the Sn-free system, where a value close to 0.494 is reached asymptotically at the highest Fe content without experiencing any discontinuity [35], in the Sn-filled system $(y + z)$ assumes a more or less constant value close to 0.492 up to Fe54_Sn, and increases sharply at higher Fe content, thus highlighting the occurrence of a discontinuity at the crossover. The trend of $(y + z)$ in the Sn-free and Sn-doped samples is reported in Fig. 17 as a function of the Fe content. As a final observation, it can also be noted that the skutterudite decomposition temperature, represented in the inset to Fig. 7, also shows a peculiar trend consisting in a linear increase up to $x = 0.54$, followed by a series of lower and roughly constant temperature values around 980 K, indicating once again the presence of a discontinuity in the vicinity of the p/n crossover.

The discussion of the thermoelectric properties of the studied system should include comparison with other similar skutterudite-based systems. Typically, comparisons will be made with Sn-free systems having

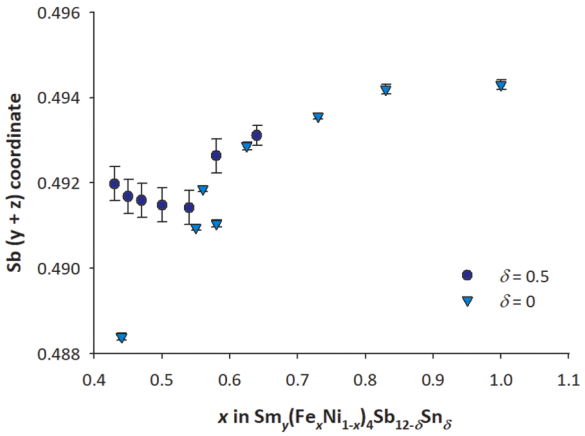

Fig. 17. Trend of the sum of Sb fractional coordinates y and z in Sn-free and Sn-doped samples as a function of the Fe content x. Data of Sn-free samples are reproduced from ref. [27].

the same or another trivalent rare earth as a filler ion and a Fe/Ni content close to that of the samples studied in this work, in order to highlight the effect of the partial substitution at the Sb position. Such systems are for example $Yb_yFe_{0.5}Ni_{0.5}Sb_{12}$ [37], $DD_yFe_xNi_{1-x}Sb_{12}$ [38], $Sm_yFe_xNi_{1-x}Sb_{12}$ [40], $(Ba,DD,Yb)_y(Fe_xNi_{1-x})Sb_{12}$ [41], and $(Ce,Yb)_y(Fe_xNi_{1-x})_4Sb_{12}$ with $x = 0.51$ [77]. The comparison between the present and other Sn-doped systems, on the contrary, is not straightforward, since information on other Sn- (or Ge-) doped (Fe,Ni)-based skutterudites is not available in the literature, to our knowledge. The differences in thermoelectric properties should in fact be attributable both to the presence of Sn (or Ge), and to the different electronic count due to the presence of transition metals other than Fe and Ni. For this reason, this comparison will generally be avoided.

With reference to the Seebeck coefficient *S*, it can be noted that the trend of this parameter as a function of temperature is strictly connected to that of other (Fe,Ni)-based skutterudites doped with trivalent filler ions. In the case of $DD_yFe_xNi_{1-x}Sb_{12}$ [38], for example, there is a close similarity between the behaviour of the sample with $x = 0.5$ and that of the Sn-doped sample with $x = 0.45$ and $x = 0.47$ described in this work: all these compositions are *n*-conductors, and are similar both in terms of *S* value and behaviour as a function of temperature, with a minimum localized in the vicinity of 500 K. The reason behind this evidence is to be found in the electronic count of the two systems: for a given *x*, the presence of Sn shifts the filler content toward higher values, as evident in Fig. 6. In other words, the electronic count of a certain Sn-free sample is achieved in Sn-doped samples at a slightly lower *x*, reflecting in the result described. A substantially different trend is presented, on the contrary, by samples belonging to the $Yb_yFe_{0.5}Ni_{0.5}Sb_{12}$ system [37]: all of them are *n*-conductors, but with significantly different values of *S*, as a consequence of the different amount of Yb introduced into the cell, and of the different oxidation state of Yb, which can assume either the trivalent or the divalent oxidation state. Consequently, in the $(Ba,DD,Yb)_y(Fe_xNi_{1-x})Sb_{12}$ system [41], the lower electron contribution of the bivalent Ba makes the composition with $x = 0.52$ a *p*-conductor.

Regarding electrical resistivity, it can be observed that for $x = 0.5$, the electrical resistivity is higher in our Sn-doped samples than in the Sn-free and DD-doped ones belonging to the $DD_yFe_xNi_{1-x}Sb_{12}$ system [38]. This evidence can be explained considering the lower number of charge carriers occurring in Sn-doped samples due to the proximity of $x = 0.5$ to the *x* value corresponding to the *p*/*n* crossover, which is found at $x \sim 0.54$, as previously described. This behaviour is also well confirmed by the resistivity values displayed by $Sm_yFe_xNi_{1-x}Sb_{12}$ with $x = 0.5$ [40], which are similar to those of the $DD_yFe_xNi_{1-x}Sb_{12}$ system. Conversely, the resistivity value of the Sn-doped sample with $x = 0.5$ is consistent with that of $(Ce,Yb)_y(Fe_xNi_{1-x})_4Sb_{12}$ with $x = 0.51$ [77], most likely due to the presence of Yb, which occurs in a mixed 2+/3+ oxidation state [78], thus providing a lower number of charge carriers compared to the Sm- and the DD-filled system.

According to the data reported in Fig. 12, a particularly low overall thermal conductivity is exhibited by Fe45_Sn and Fe54_Sn, *i.e.* by the compositions in the immediate vicinity of the *p*/*n* crossover. In comparison to all studied compositions in the system $DD_yFe_xNi_{1-x}Sb_{12}$ [38], $Yb_xFe_2Ni_2Sb_{12}$ [37] and $(Sm,Gd)_yFe_xNi_{1-x}Sb_{12}$ [40], the Sn-doped samples exhibit a lower *k* at each temperature; the same can be said also for k_{ph}, at least where this value is explicitly calculated, *i.e.* for $DD_yFe_xNi_{1-x}Sb_{12}$ and $(Sm,Gd)_yFe_xNi_{1-x}Sb_{12}$. A further comparison can be made with Sn-doped samples belonging to other skutterudite systems, such as $Nd_{0.6}Fe_2Co_2Sb_{12-x}Sn_x$ [53] and $DD_yFe_xCo_{1-x}Sb_{12-\delta}Sn_\delta$ [42], which show thermal conductivity values in good agreement with those of the samples studied in this work.

The analysis of *ZT* as a function of temperature allows us to draw some conclusions. As mentioned above, the *ZT* data of all the samples considered present a maximum occurring at a temperature that depends on the proximity to the *p*/*n* crossover. As already noted, the temperature trend where the *ZT* maximum occurs follows that of *PF*, which in turn resembles that of *S*; this feature is visible in Fig. 11. Focusing on the absolute value of the maximum *ZT* (ZT_{max}) exhibited by each sample, the data presented in Fig. 14 show that ZT_{max} varies between ~ 0.15 (Fe64_Sn) and ~ 0.45 (Fe45_Sn). Comparing these data with those of the corresponding Sn-free system, it results that all the compositions considered in the present study have a higher ZT_{max} than the Sn-free system with $x = 0.50$ ($ZT_{max} \sim 0.1$ [40]), with some compositions (Fe45_Sn, Fe47_Sn, Fe54_Sn) showing a much higher value. Furthermore, the three last-mentioned compositions show a ZT_{max} value comparable to that of the Sn-free sample with $x = 0.80$, *i.e.* a *p*-conducting sample: this is a particularly appreciable result, since in (Fe,Ni)-based filled skutterudites it is known that *p*-conducting compositions are characterized by significantly higher *PF* and *ZT* values [79]. The comparison with other (Fe,Ni)-based skutterudites highlights that all ZT_{max} values of the Sn-doped samples are higher than those of $DD_{0.08}Fe_2Ni_2Sb_{12}$ [38], $Yb_yFe_2Ni_2Sb_{12}$ [37], and $(Ce,Yb)_yFe_{2.8}Ni_{1.2}Sb_{12}$ [77]. Interestingly, the composition with $x = 0.54$ has a ZT_{max} even higher than $DD_{0.40}Fe_{2.8}Ni_{1.2}Sb_{12}$ [38], again a *p*-conducting skutterudite. It can therefore be concluded that partial substitution of Sb by Sn induces an improvement of the thermoelectric properties of the corresponding Sn-free skutterudite system, mainly in terms of lowering of k_{ph} and enhancement of *ZT*, as expected by the introduction of additional scattering centers in the structure.

5. Conclusions

A systematic study of the filled skutterudite $Sm_y(Fe_xNi_{1-x})_4Sb_{11.5}Sn_{0.5}$ was conducted with the aim of determining the role of Sn in modifying the structural and thermoelectric properties of the system. Seven samples belonging to the above system with *x* ranging between 0.43 and 0.64, and *y* ranging between 0.17 and 0.34 were synthesized by the melt-quench-annealing technique. The morphology, crystal structure, thermodynamic stability and thermoelectric properties of the samples were analyzed.

Three main conclusions can be drawn.

- The *p*/*n* crossover shifts from $x \sim 0.63$ to $x \sim 0.54$ when passing from the Sn-free to the Sn-doped system, because of the smaller number of electrons provided by Sn compared to Sb, which requires a larger electron contribution from the filler atom.
- A discontinuity in the cell parameter, as well as the decomposition temperature, occurs at the *p*/*n* crossover. This evidence, also observed in the corresponding Sn-free system, marks the correlation between electronic and structural properties of the material.
- A significant increase in *ZT* occurs compared to the corresponding and other similar Sn-free systems as a consequence of the lower thermal conductivity induced by the presence of Sn, responsible for the creation of new scattering centers.

As a general conclusion, it can be stated that the partial substitution of the pnictide atom by an aliovalent atom influences the electronic, structural and thermoelectric properties of the studied filled skutterudite; in particular, the creation of new scattering centers interacting with heat-carrying phonons is effective in improving the thermoelectric properties of the material.

CRediT authorship contribution statement

Nadia Parodi: Writing – review & editing, Investigation. **Carlo Fanciulli:** Writing – review & editing, Investigation. **Roberto Spotorno:** Writing – review & editing, Investigation. **Paolo Mele:** Writing – review & editing, Investigation. **Paolo Scardi:** Writing – review & editing, Resources. **Tanguy Bernard:** Writing – review & editing, Investigation. **Ketan Lohani:** Writing – review & editing, Investigation. **Pietro Manfrinetti:** Writing – review & editing, Investigation. **Giovanna Latronico:** Writing – review & editing, Investigation. **Cecilia Piscino:** Writing – review & editing, Writing – original draft,

Visualization, Investigation, Formal analysis. **Cristina Artini:** Writing – review & editing, Writing – original draft, Visualization, Supervision, Conceptualization.

Declaration of Competing Interest

The authors declare that they have no known competing financial interests or personal relationships that could have appeared to influence the work reported in this paper.

Acknowledgements

P. Scardi & T. Bernard acknowledge the Italian Ministry of Universities and Research (MUR), in the framework of the project DICAM-EXC (Department of Excellence 2023-2027, grant L232/2016).

Appendix A. Supporting information

Supplementary data associated with this article can be found in the online version at doi:10.1016/j.jallcom.2024.176966.

Data availability

Data will be made available on request.

References

[1] C. Artini, et al., Roadmap on thermoelectricity, Nanotechnology 34 (2023) 292001.
[2] F. Laghzal, S. Id Mbairi, A. Tihane, A. Alsaad, A. Narjis, Comprehensive overview on thermoelectricity –materials, applications and recent advances, Mater. Sci. Eng. B 307 (2024) 117512.
[3] P. Baskaran, M. Rajasekar, Recent trends and future perspectives of thermoelectric materials and their applications, RSC Adv. 14 (2024) 21706–21744.
[4] R. Singh, S. Dogra, S. Dixit, N. Ivanovich Vatin, R. Bhardwaj, A.K. Sundramoorthy, H.C.S. Perera, S.P. Patole, Rajneesh Kumar Mishra, S. Arya, Advancements in thermoelectric materials for efficient waste heat recovery and renewable energy generation, Hybrid. Adv. 5 (2024) 100176.
[5] Y. Tian, G.-K. Ren, Z. Wei, Z. Zheng, S. Deng, L. Ma, Y. Li, Z. Zhou, X. Chen, Y. Shi, Y.-H. Lin, Advances of thermoelectric power generation for room temperature: applications, devices, materials and beyond, Renew. Energy 226 (2024) 120443.
[6] D. Palaporn, S. Tanusilp, Y. Sun, S. Pinitsoontorn, K. Kurosaki, Thermoelectric materials for space explorations, Mater. Adv. 5 (2024) 5351–5364.
[7] R. Manghwar, J. Selvaraj, N. Abd Rahim, L. Kumar, H. Khoharo, Global advancements of solar thermoelectric generators application, limitations, and prospects: a comprehensive review, Appl. Therm. Eng. 257 (2024) 124231.
[8] J. Wang, L. Lu, K. Jiao, Solar- and/or radiative cooling-driven thermoelectric generators: a critical review, Energy Eng. 121 (2024) 2681–2718.
[9] C. Li, Y. Luo, W. Li, B. Yang, C. Sun, W. Ma, Z. Ma, Y. Wei, X. Li, J. Yang, The on-chip thermoelectric cooler: advances, applications and challenges, Chip 3 (2024) 100096.
[10] L. Huang, Y. Zheng, L. Xing, B. Hou, Recent progress of thermoelectric applications for cooling/heating, power generation, heat flux sensor and potential prospect of their integrated applications, Therm. Sci. Eng. Prog. 45 (2023) 102064.
[11] M.Dinesh Kadam, P.M. Gore, B. Kandasubramanian, Fiber-based thermoelectric generators and their substrate materials, Hybrid. Adv. 5 (2024) 100177.
[12] M. Jabri, S. Masoumi, F. Sajadirad, R.P. West, A. Pakdel, Thermoelectric energy conversion in buildings, Mater. Today Energy 32 (2023) 101257.
[13] S.W. Sharshir, A. Joseph, M.M. Elsayad, A.W. Kandeal, A.S. Abdullah, C. Wang, S.-H. Jang, M. An, N.M. Ghazaly, Z. Yuan, Energy harvesting via thermoelectric generators for green hydrogen production: methods and techniques, Process Saf. Environ. Prot. 190 (2024) 443–463.
[14] P. Baskaran, M. Rajasekar, Recent trends and future perspectives of thermoelectric materials and their applications, RSC Adv. 14 (2024) 21706–21744.
[15] J. Feng, J. Li, R. Liu, Low-temperature thermoelectric materials and applications, Nano Energy 126 (2024) 109651.
[16] A. Bugalia, V. Gupta, N. Thakur, Strategies to enhance the performance of thermoelectric materials: a review, J. Renew. Sustain. Energy 15 (2023) 032704.
[17] C.D. Zhou, B. Liang, W.J. Huang, J.G. Noudem, X.J. Tan, J. Jiang, Phonon engineering significantly reducing thermal conductivity of thermoelectric materials: a review, Rare Met. 42 (2023) 2825–2839.
[18] G.A. Slack, New materials and performance limits for thermoelectric cooling, in: D. M. Rowe (Ed.), CRC Handbook of Thermoelectrics, Taylor and Francis, Boca Raton, USA, 1995.
[19] M.Sehar Abbasi, R. Sultana, I. Ahmed, M. Adnan, U.Ali Shah, M.Sultan Irshad, H. Ngoc Vu, L. Thi Do, H.Ha Thi Vu, T.-D. Pham, H.Xuan Nang, V.-D. Dao, Contemporary advances in organic thermoelectric materials: fundamentals, properties, optimization strategies, and applications, Renew. Sust. Energ. Rev. 200 (2024) 114579.
[20] A. Ojha, R.Krushna Sabat, S. Bathula, Advancement in half-Heusler thermoelectric materials and strategies to enhance the thermoelectric performance, Mater. Sci. Semicond. Process. 171 (2024) 107996.
[21] G. Rogl, P.F. Rogl, Development of thermoelectric half-heusler alloys over the past 25 years, Crystals 13 (2023) 1152.
[22] J. Zheng, M. Ma, G. Yang, Y. Wu, D. Mei, Progress in the study of binary chalcogenide-based thermoelectric compounds, J. Solid State Chem. 334 (2024) 124617.
[23] M.R. Shankar, A.N. Prabhu, A review on structural characteristics and thermoelectric properties of mid-temperature range chalcogenide-based thermoelectric materials, J. Mater. Sci. 58 (2023) 16591–16633.
[24] K. Kishimoto, K. Akai, Thermoelectric properties of type-I clathrate $Na_8Al_8Ge_{38}$, J. Solid State Chem. 324 (2023) 124122.
[25] R. Moshwan, X.-L. Shi, W.-D. Liu, J. Liu, Z.-G. Chen, Entropy engineering: an innovative strategy for designing high-performance thermoelectric materials and devices, Nano Today 58 (2024) 102475.
[26] S. Ghosh, L. Raman, S. Sridar, W. Li, High-entropy engineering in thermoelectric materials: a review, Crystals 14 (2024) 432.
[27] C. Uher, Skutterudite-Based Thermoelectrics, in: D.M. Rowe (Ed.), Thermoelectrics Handbook – Macro to Nano, Taylor and Francis, Boca Raton, USA, 2006.
[28] B.C. Sales, Filled skutterudites, in: K.A. Gschneidner Jr, J.-C. G. Bünzli, V.K. Pecharsky (Eds.), Handbook on the Physics and Chemistry of Rare Earths, North Holland, Amsterdam, Netherlands, 2003, Volume 33, pp. 1-34.
[29] A. Saini, U.Farooq Lone, An analysis of thermoelectric properties of skutterudites, Phys. Status Solidi B 261 (2024) 2300244.
[30] P. Rawat, M.Ho Lee, A. Kumar, S. Thoravat, J.Soo Rhyee, Thermoelectric properties of extrinsic phase mixing in chalcogenide bulk nanocomposites, Curr. Appl. Phys. 60 (2024) 15–31.
[31] U. Ijaz, M. Siyar, C. Park, The power of pores: review on porous thermoelectric materials, RSC Sustain 2 (2024) 852–870.
[32] J. Dong, A. Suwardi, X.Yi Tan, N. Jia, K. Saglik, R. Ji, X. Wang, Q. Zhu, J. Xu, Q. Yan, Challenges and opportunities in low-dimensional thermoelectric nanomaterials, Mater. Today 66 (2023) 137–157.
[33] G. Latronico, P. Mele, C. Artini, P. Manfrinetti, C. Fanciulli, S.Pian Wei, Y. Kawamura, C. Sekine, S. Singh, T. Takeuchi, T. Baba, C. Bourgès, T. Mori, Investigation on the power factor of skutterudite $Sm_y(Fe_xNi_{1-x})_4Sb_{12}$ thin films: effects of deposition and annealing temperature, Materials 14 (2021) 5773.
[34] G. Latronico, P. Mele, C. Sekine, P.Sian Wei, S. Singh, T. Takeuchi, C. Bourgès, T. Baba, T. Mori, P. Manfrinetti, C. Artini, Effect of the annealing treatment on the structural and transport properties of thermoelectric $Sm_y(Fe_xNi_{1-x})_4Sb_{12}$ thin films, Nanotechnology 34 (2023) 115705.
[35] C. Artini, G. Zanicchi, G.A. Costa, M.M. Carnasciali, C. Fanciulli, R. Carlini, Correlations between structural and electronic properties in the filled skutterudite $Sm_y(Fe_xNi_{1-x})_4Sb_{12}$, Inorg. Chem. 55 (2016) 2574–2583.
[36] T. Morimura, M. Hasaka, Partially filled skutterudite structure in $Ce_fFe_{8-x}Ni_xSb_{24}$, Scr. Mater. 48 (2003) 495–500.
[37] A. Kaltzoglou, P. Vaqueiro, K.S. Knight, A.V. Powell, Synthesis, characterization and physical properties of the skutterudites $Yb_xFe_2Ni_2Sb_{12}$ ($0 \leq x \leq 0.4$), J. Solid State Chem. 193 (2012) 36–41.
[38] G. Rogl, A. Grytsiv, E. Bauer, P. Rogl, M. Zehetbauer, Thermoelectric properties of novel skutterudites with didymium: $DD_y(Fe_{1-x}Co_x)_4Sb_{12}$ and $DD_y(Fe_{1-x}Ni_x)_4Sb_{12}$, Intermetallics 18 (2010) 57–64.
[39] B. Bourgouin, D. Bérardan, E. Alleno, C. Godart, O. Rouleau, E. Leroy, Preparation and thermopower of new mischmetal-based partially filled skutterudites $Mm_yFe_{4-x}(Co/Ni)_xSb_{12}$, J. Alloy Compd. 399 (2005) 47–51.
[40] C. Artini, R. Carlini, R. Spotorno, F. Failamani, T. Mori, P. Mele, Structural properties and thermoelectric performance of the double filled skutterudite $(Sm, Gd)_y(Fe_xNi_{1-x})_4Sb_{12}$, Materials 12 (2019) 2451.
[41] G. Rogl, A. Grytsiv, E. Royanian, P. Heinrich, E. Bauer, P. Rogl, M. Zehetbauer, S. Puchegger, M. Reinecker, W. Schranz, New p- and n-type skutterudites with ZT>1 and nearly identical thermal expansion and mechanical properties, Acta Mater. 61 (2013) 4066–4079.
[42] G. Rogl, A. Grytsiv, P. Heinrich, E. Bauer, P. Kumar, N. Peranio, O. Eibl, J. Horky, M. Zehetbauer, P. Rogl, New bulk p-type skutterudites $DD_{0.7}Fe_{2.7}Co_{1.3}Sb_{12-x}X_x$ (X = Ge, Sn) reaching ZT > 1.3, Acta Mater. 91 (2015) 227–238.
[43] F. Duan, L. Zhang, J. Dong, J. Sakamoto, B. Xu, X. Li, Y. Tian, Thermoelectric properties of Sn substituted p-type Nd filled skutterudites, J. Alloy Compd. 639 (2015) 68–73.
[44] J.-S. Kim, D.-K. Shin, K.-H. Park, I.-H. Kim, Skutterudite: reproducibility of thermoelectric performance of P-type $R_{yF}e_{4-x}Co_xSb_{12}$ bulky compacts, Korean J. Met. Mater. 62 (2024) 542–549.
[45] X. Cao, M. He, B. Ma, S. Liu, X. Pang, M. Song, F. Zhang, X. Chao, Z. Yang, D. Wu, Enhanced thermoelectric properties of Mm-filled p-type $(Fe,Co)Sb_3$ skutterudites via Co/Fe ratio regulation and extra Sb compensation, J. Alloy. Compd. 972 (2024) 172815.
[46] L. Kong, X. Jia, Y. Zhang, B. Sun, B. Liu, H. Liu, C. Wang, B. Liu, J. Chen, H. Ma, N-type $Ba_{0.3}Ni_{0.15}Co_{3.85}Sb_{12}$ skutterudite: high pressure processing technique and thermoelectric properties, J. Alloy Compd. 734 (2018) 36–42.
[47] X. Fan, D. Zhou, Y. Chen, X. Li, S. Gao, W. Ji, Y. Zhang, Q. Chen, H. Ma, X. Jia, High-pressure and high-temperature synthesis of stable $S_xCo_{3.6}Ni_{0.4}Sb_{12}$ skutterudite compounds, Ceram. Int. 49 (2023) 6299–6306.
[48] D. Li, X.-L. Shi, J. Zhu, M. Li, J. Wang, W.-D. Liu, Q. Zhao, H. Zhong, S. Li, Z.-G. Chen, Ce-filled $Ni_{1.5}Co_{2.5}Sb_{12}$ skutterudite thin films with record-high figure of merit and device performance, Adv. Energy Mater. 13 (2023) 2301525.
[49] L. Chapon, D. Ravot, J.C. Tedenac, Nickel-substituted skutterudites: synthesis, structural and electrical properties, J. Alloy Compd. 282 (1999) 58–63.

[50] C. Artini, A. Castellero, M. Baricco, M.T. Buscaglia, R. Carlini, Structure, microstructure and microhardness of rapidly solidified $Sm_y(Fe_xNi_{1-x})_4Sb_{12}$ (x = 0.45, 0.50, 0.70, 1) thermoelectric compounds, Solid State Sci. 79 (2018) 71–78.
[51] D. Bérardan, E. Alleno, C. Godart, O. Rouleau, J. Rodriguez-Carvajal, Preparation and chemical properties of the skutterudites $(Ce\text{-}Yb)_yFe_{4-x}(Co/Ni)_xSb_{12}$, Mater. Res. Bull. 40 (2005) 537–551.
[52] F. Duan, L. Zhang, J. Dong, J. Sakamoto, B. Xu, X. Li, Y. Tian, Thermoelectric properties of Sn substituted p-type Nd filled skutterudites, J. Alloy Compd. 639 (2015) 68–73.
[53] P. Qiu, X. Shi, X. Chen, X. Huang, R. Liu, L. Chen, Effects of Sn-doping on the electrical and thermal transport properties of p-type cerium filled skutterudites, J. Alloy Compd. 509 (2011) 1101–1105.
[54] N. Shaheen, M.Sufyan Javed, H.Ullah Shah, S. Hussain, M.Ashfaq Ahmad, R. Raza, M. Saleem, X. Zhou, Enhanced thermoelectric properties in Ge-doped and single-filled skutterudites prepared by unique melt-spinning method, Ceram. Int. 44 (2018) 12610–12614.
[55] B. Qin, Y. Ji, Y. Lei, Y. Li, Enhancing thermoelectric properties of (Cu,Te) co-doped skutterudite synthesized by solid-state reaction, Ceram. Int. 50 (2024) 28296–28300.
[56] Q. Jing, Z. Zhang, L. Deng, Q. Chen, Optimization of $Co_4Sb_{11.5}Te_{0.5}$ thermoelectric performance through Al filling under high temperature and high pressure, Ceram. Int. (2024), https://doi.org/10.1016/j.ceramint.2024.09.169.
[57] J. Dong, K. Yang, B. Xu, L. Zhang, Q. Zhang, Y. Tian, Structure and thermoelectric properties of Se- and Se/Te-doped $CoSb_3$ skutterudites synthesized by high-pressure technique, J. Alloy Compd. 647 (2015) 295–302.
[58] M.J. Kruszewski, K. Cymerman, E. Choińska, D. Moszczyńska, Ciupiński, A comparative study of oxidation behavior of Co_4Sb_{12} and $Co_4Sb_{10.8}Se_{0.6}Te_{0.6}$ skutterudite thermoelectric materials fabricated via fast SHS-PPS route, J. Eur. Ceram. Soc. 44 (2024) 3760–3766.
[59] B. Duan, P. Zhai, L. Liu, Q. Zhang, Enhanced thermoelectric performance in sulfur-doped $Co_4Sb_{11.9-x}Te_xS_{0.1}$ skutterudites, Mater. Lett. 79 (2012) 69–71.
[60] H. Sun, X. Jia, L. Deng, C. Wang, P. Lv, X. Guo, B. Sun, Y. Zhang, B. Liu, H. Ma, Beneficial effect of high pressure and double-atom-doped skutterudite compounds $Co_4Sb_{11.5-x}Te0.5Sn_x$ by HPHT, J. Alloy Compd. 612 (2014) 16–19.
[61] Y. Chen, X. Fan, S. Gao, W. Ji, X. Li, Y. Zhang, H. Ma, X. Jia, Synthesis of electronegative S-filled and Sn–Te double substituted skutterudite compounds by HPHT and its thermoelectric properties, Mod. Phys. Lett. B 38 (2024) 2350212.
[62] X. Su, H. Li, G. Wang, H. Chi, X. Zhou, X. Tang, Q. Zhang, C. Uher, Structure and transport properties of double-doped $CoSb_{2.75}Ge_{0.25-x}Te_x$ ($x = 0.125$–0.20) with in situ nanostructure, Chem. Mater. 23 (2011) 2948–2955.
[63] I.K. Dimitrov, M.E. Manley, S.M. Shapiro, J. Yang, W. Zhang, L.D. Chen, Q. Jie, G. Ehlers, A. Podlesnyak, J. Camacho, Q. Li, Einstein modes in the phonon density of states of the single-filled skutterudite $Yb_{0.2}Co_4Sb_{12}$, Phys. Rev. B 82 (2010) 174301.
[64] J.L. Feldman, D.J. Singh, Lattice dynamics of skutterudites: first-principles and model calculations for $CoSb_3$, Phys. Rev. B 53 (1996) 6273.
[65] Q. Zhang, C. Chen, Y. Kang, X. Li, L. Zhang, D. Yu, Y. Tian, B. Xu, Structural and thermoelectric characterizations of samarium filled CoSb3 skutterudites, Mater. Lett. 143 (2015) 41–43.
[66] C. Artini, R. Carlini, L. Gigli, C. Fanciulli, Compositional optimization and structural properties of the filled skutterudite $Sm_y(Fe_xNi_{1-x})_4Sb_{11.5}Sn_{0.5}$, Metals 10 (2020) 692.
[67] I.-H. Kim, K.-H. Park, S.-C. Ur, Thermoelectric properties of Sn-doped $CoSb_3$ prepared by encapsulated induction melting, J. Alloy Compd. 442 (2007) 351–354.
[68] J. Rodríguez-Carvajal, Recent advances in magnetic structure determination by neutron powder diffraction, Phys. B 192 (1993) 55–69.
[69] P. Villars, K. Cenzual, Pearson's Crystal Data: Crystal Structure Database for Inorganic Compounds (on DVD), Release 2022/23, ASM International, Materials Park, Ohio, USA.
[70] H.J. Goldsmid, J.W. Sharp, Estimation of the thermal band gap of a semiconductor from Seebeck measurements, J. Electron. Mater. 28 (1999) 869–872.
[71] G. Rogl, A. Grytsiv, M. Falmbigl, E. Bauer, P. Rogl, M. Zehetbauer, Y. Gelbstein, Thermoelectric properties of p-type didymium (DD) based skutterudites $DD_y(Fe_{1-x}Ni_x)_4Sb_{12}$ ($0.13 \le x \le 0.25$, $0.46 \le y \le 0.68$), J. Alloy Compd. 537 (2012) 242–249.
[72] H.-S. Kim, Z.M. Gibbs, Y. Tang, H. Wang, G.J. Snyder, Characterization of Lorenz number with Seebeck coefficient measurement, APL Mater. 3 (2015) 041506.
[73] C. Artini, N. Parodi, G. Latronico, R. Carlini, Formation and decomposition process of the filled skutterudite $Sm_y(Fe_xNi_{1-x})_4Sb_{12}$ ($0.40 \le x \le 1$) as revealed by differential thermal analysis, J. Mater. Eng. Perform. 27 (2018) 6259–6265.
[74] K.W. Richter, H. Ipser, An experimental investigation of the Fe-NiSb ternary phase diagram, J. Phase Equilib. 18 (1997) 235–244.
[75] I. Oftedal, The crystal structure of skutterudite and related minerals, Nor. Geol. Tidsskr. 8 (1926) 250–257.
[76] A. Kjekshus, D.G. Nicholson, T. Rakke, Compounds with the skutterudite type crystal structure. I. on oftedal's relation, Acta Chem. Scand. 27 (1973) 1307–1314.
[77] D. Bérardan, E. Alleno, C. Godart, M. Puyet, B. Lenoir, R. Lackner, E. Bauer, L. Girard, D. Ravot, Improved thermoelectric properties in double-filled $Ce_{y/2}Yb_{y/2}Fe_{4-x}(Co/Ni)_xSb_{12}$ skutterudites. J. Appl. Phys. 98 (2005) 033710.
[78] D. Bérardan, C. Godart, E. Alleno, E. Bauer, Chemical properties and thermopower of the new series of skutterudite $Ce_{1-p}Yb_pFe_4Sb_{12}$, J. Alloy Compd. 351 (2003) 18–23.
[79] C. Artini, G. Latronico, R. Carlini, S. Saini, T. Takeuchi, S. Choi, A. Baldini, U. Anselmi-Tamburini, F. Valenza, P. Mele, Effect of different processing routes on the power factor of the filled skutterudite Smy(FexNi1-x)4Sb12, ES Mater. Manuf. 5 (2019) 29–37.